Ferroelectricity in oxygen-terminated two-dimensional carbides of lanthanide elements

Lin Han,[1] Wencong Sun,[1] Pingwei Liu,[1] Xianqing Lin,[2] Dan Liu,[1,*] and David Tománek[3,4,†]

[1]*School of Physics, Southeast University, Nanjing, 211189, People's Republic of China*

[2]*College of Science, Zhejiang University of Technology, Hangzhou, 310023, People's Republic of China*

[3]*Physics and Astronomy Department, Michigan State University, East Lansing, Michigan 48824, USA*

[4]*Department of Physics, University of Johannesburg, 2006 Auckland Park, South Africa*

(Received 8 December 2023; revised 31 March 2024; accepted 10 May 2024; published 30 May 2024)

We investigate the properties of oxygen-functionalized carbides of lanthanide elements with the composition M_2CO_2 (M = Gd, Tb, Dy) that form two-dimensional structures. Our *ab initio* calculations reveal that oxygen termination turns M_2C monolayers into semiconductors with two dynamically stable phases. Of these, the energetically favored α phase becomes ferroelectric, whereas the β phase turns antiferroelectric. Applying in-plane biaxial strain may transform one phase into the other, changes the ferroelectric polarization of the α phase in a linear fashion, and modifies the size and nature of the fundamental band gap from direct to indirect. The structure with a direct band gap exhibits in-plane isotropic electronic and optical properties. This previously unexplored class of systems also exhibits excellent photon absorption in the ultraviolet range.

DOI: 10.1103/PhysRevMaterials.8.054005

I. INTRODUCTION

Since the discovery of ferroelectricity in Rochelle salt in 1920s [1,2], ferroelectric materials have captured ample attention of the scientific community due to their complex behavior and unique applicability in electronic devices. The interest in two-dimensional (2D) materials, ignited by the successful exfoliation of graphene, led to the exploration of ferroelectricity not only in three-dimensional (3D) materials, but also in lower dimensions. Early studies focused on intrinsic ferroelectric behavior in 2D compounds including In_2Se_3 [3,4], $CuInP_2S_6$ [5,6], and in elemental materials such as 2D α- or δ-Se [7]. Among the plethora of 2D structures, however, only very few have been found to exhibit intrinsic ferroelectric behavior. With few 2D systems available that show ferroelectric behavior, which moreover is not very interesting, hope for useful applications of 2D ferroelectrics started to dwindle. A useful change appeared when intrinsically nonferroelectric 2D materials were decorated by functional radicals that induce ferroelectric behavior. This was first demonstrated when graphene turned ferroelectric following the functionalization by OH groups [8]. Functionalization by different radicals offers almost unlimited possibilities to fabricate 2D ferroelectrics. In this paper, we focus on 2D electrides consisting of carbides of lanthanide elements that are terminated by oxygen.

Electrides form a family of materials where interstitial anionic electrons are trapped in cavities within the sublattice of positive ions [9–13]. In 2013, layered electride Ca_2N was successfully synthesized [9] and Ca_2N monolayers were subsequently isolated in 2016 using liquid exfoliation [14]. Since then, various 2D layered electrides have been synthesized experimentally or predicted theoretically [15–23]. However, these layered electrides are only stable under very specific conditions. These include a nitrogen atmosphere or selected organic solvents for monolayers of Ca_2N [14], ultrahigh vacuum conditions for Y_2C [16], and high-purity Ar environment for Gd_2C [17]. The presence of highly delocalized electrons, which are trapped in between individual layers, make these materials very reactive. Exposure to air leads to undesirable property changes due to the oxidation of $-$Cl, $-$OH, $-$H, and $-$F functional groups [24–34]. Sensitivity to specific environments has also been observed regarding magnetic polarization. For example, $-$Cl or $-$Br termination of Gd_2C causes antiferromagnetism with out-of-plane Néel ordering, whereas termination by $-$I leads to a zigzag antiferromagnetic (AFM) ordering [34]. Not only magnetic, but also electronic properties can be modified and tuned by different functional groups. Monolayers of Gd_2C [33] become semimetallic when covered by hydrogen on one side, but turn insulating when hydrogen covers both sides. With this richness in behavior, we expect that ferroelectricity can be induced in many 2D compounds by specific functional groups.

Our paper investigates previously unexplored carbides of lanthanide elements with the composition M_2C (M = Gd, Tb, Dy), which form 2D structures. Our *ab initio* calculations show that termination of these 2D compounds by oxygen to M_2CO_2 turns these systems into ferroelectrics. We find two stable phases of these systems with different ferroelectric properties. The ferroelectric α phase with out-of-plane polarization is generally more stable than the antiferroelectric β phase. We focus mainly on the α phase, which may be of interest for applications, and discuss its relation to the β phase with a sublattice of flipped dipoles. Semiconducting $\alpha - M_2CO_2$ has an indirect fundamental band gap that can turn to a direct gap by applying specific in-plane biaxial strain, which also monotonically changes the polarization.

*liudan2@seu.edu.cn

†tomanek@msu.edu

Our results also reveal excellent photoabsorption capability of the direct-gap M_2CO_2 system, which increases its value for applications.

II. COMPUTATIONAL TECHNIQUES

Our calculations of the atomic structure, electronic, and optical properties have been performed using the density functional theory (DFT) as implemented in the VASP [35,36] code. We used the Perdew-Burke-Ernzerhof (DFT-PBE) [37] exchange-correlation functional for most of the study. Specific calculations of the band structure and the optical absorption coefficient were performed using the hybrid DFT-HSE06 functional [38,39] with the default mixing parameter $\alpha = 0.25$. Periodic boundary conditions have been used throughout the study, with monolayers represented by a periodic array of slabs separated by a 20-Å-thick vacuum region. The calculations were performed using the projector augmented wave (PAW) method [36] and a 520 eV energy cutoff. The 2D Brillouin zone (BZ) in the reciprocal space has been sampled by a fine $10\times10\times1k$-point grid in the α phase and $10\times6\times1$ k-point grid in the β phase [40]. All geometries have been optimized using the conjugate gradient (CG) method [41], until none of the residual Hellmann-Feynman forces exceeded 10^{-2} eV/Å. The polarization was calculated using the standard Berry phase approach [42,43] as implemented in the VASP code. The phonon spectrum was determined using $4\times4\times1$ supercells, and the real-space force constants in the supercells were calculated using the density-functional perturbation theory (DFPT) as implemented in VASP [44].

III. RESULTS

A. Atomic structure and stability of O − terminated 2D lanthanide carbides M_2CO_2

We find O − terminated 2D lanthanide carbide structures with the composition M_2CO_2 (M = Gd, Tb, Dy) to be stable. Specific results for Gd-based systems are presented in the main text and those for Tb- and Dy-based systems in the Appendixes.

Thin slabs of Gd_2C contain three atomic layers. Gd atoms form the top and bottom layers and are separated equidistantly by a C layer in the middle. Since the Gd_2C layer is chemically unstable in air [17], we studied a potentially more stable compound formed by oxidizing both surfaces of Gd_2C. We found two stable allotropes of Gd_2CO_2, namely, the α phase shown in Fig. 1(a) and the β phase shown in Fig. 1(b). Since Tb and Dy are neighbors of Gd in the lanthanoid series, their compounds show similar chemical behaviors and physical properties as those of Gd.

The optimum lattice constant in the α phase is $a = a_1 = a_2 = 3.77$ Å. In the β phase, the optimum lattice constants are $a_1 = 3.70$ Å and $a_2 = 6.44$ Å. Based on DFT-PBE results, the α phase of M_2CO_2 is more stable than the β phase by 29 meV/unit cell for M = Gd, 26 meV/unit cell for M = Tb, and 25 meV/unit cell for the Dy-based compound. In all systems, the C atoms have moved from their initial central position in-between the M layers. In the α phase, all of the C atoms bond to O atoms in one of the terminating layers and acquire a net positive charge. The carbon layer remains planar,

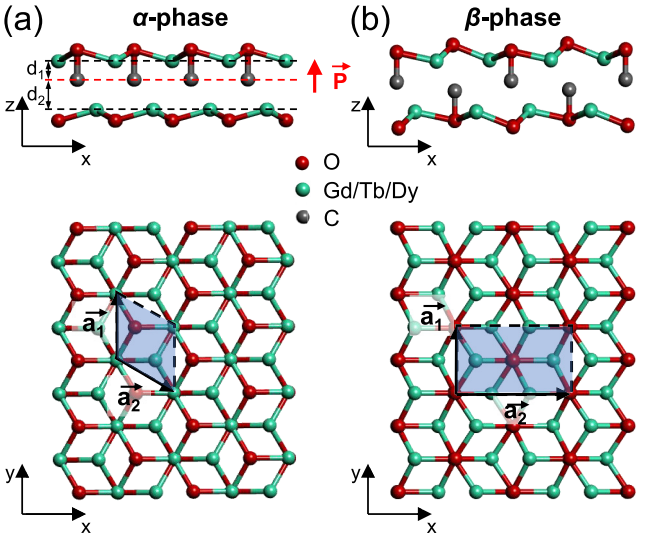

FIG. 1. Atomic structure of 2D M_2CO_2 (M = Gd, Tb, Dy) in the (a) α and (b) β phases. The unit cells of the 2D structures are highlighted by the transparent blue areas. $a = a_1 = a_2$ is the length of the equally long Bravais lattice vectors in the α phase. The direction of the electric polarization is indicated by the red arrows.

but is no longer equidistant to the terminating M layers. As seen in the top panel of Fig. 1(a), its separation d_1 from one terminating M layer is shorter than the separation d_2 from the other terminating layer. We characterize the deviation from equidistance by the quantity $\Delta d = (d_2 - d_1)/2$. The α phase shows a $P3m1$ symmetry and exhibits a net out-of-plane electric polarization.

In the β phase with $P2_1/m$ symmetry, the C atoms in the middle layer bond alternatively to oxygen atoms in one or the other terminating M layer. As seen in the upper panel of Fig. 1(b), the carbon layer is no longer planar. The local polarization changes along the alternating displacement direction of the C atoms. As a result, the β phase exhibits zero net polarization.

We also calculated the phonon spectra of the two Gd_2CO_2 phases and present the phonon band structure in Fig. 2. The frequency spectrum of both phases is free of imaginary frequencies, which means that both allotropes are dynamically stable. We reach the same conclusion about the dynamical

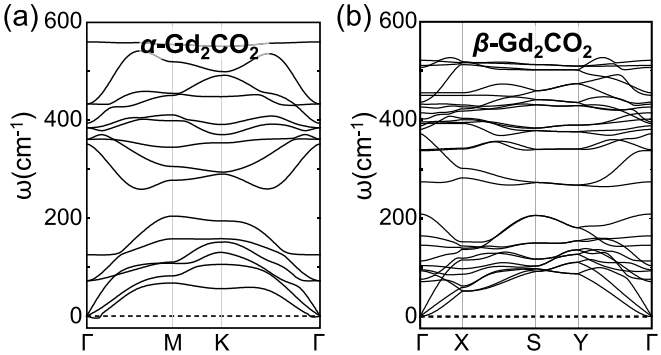

FIG. 2. Phonon spectrum of (a) $\alpha - Gd_2CO_2$ and (b) $\beta - Gd_2CO_2$.

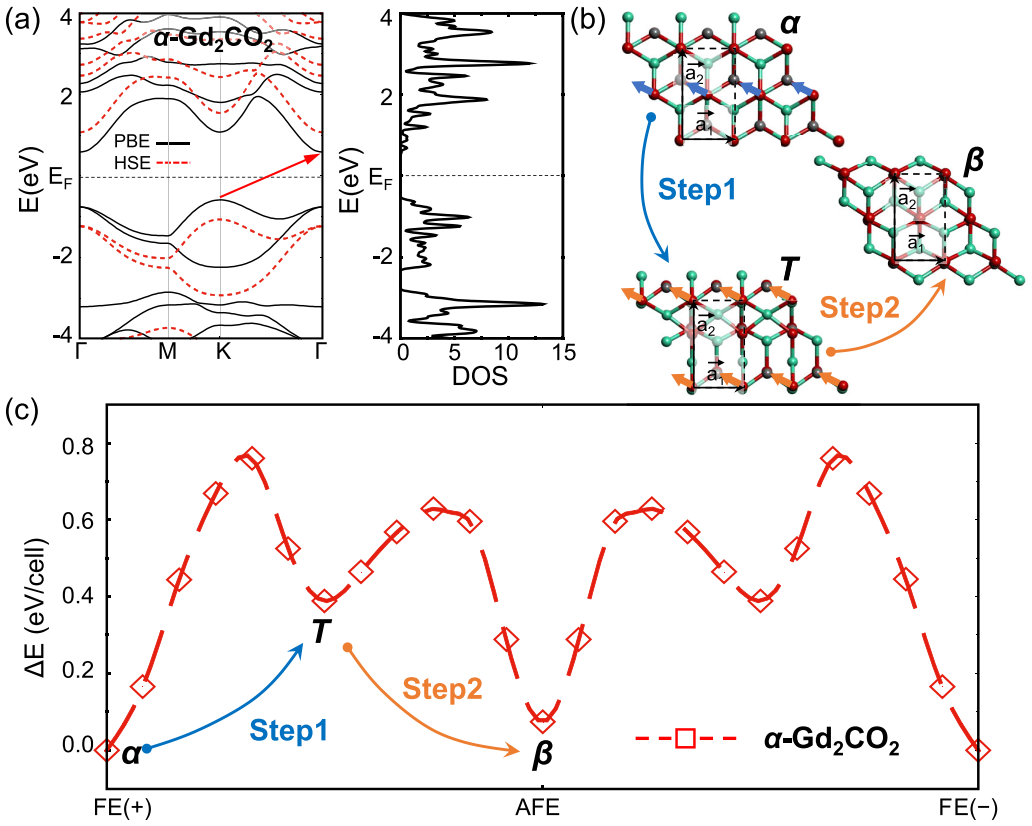

FIG. 3. (a) Electronic band structure $E(k)$ and density of states (DOS) of $\alpha - Gd_2CO_2$. Results based on DFT-PBE are represented by the solid black lines and DFT-HSE06 results by the dashed red lines. (b) Illustration of the transformation process from $\alpha - Gd_2CO_2$ to $\beta - Gd_2CO_2$. Starting from the initial α phase, displacement of O atoms, indicated by the green arrows, leads to the transition phase (T phase). Subsequent displacement of the O atoms along the direction of the yellow arrows moves the system to the β phase. (c) Energy changes ΔE per unit cell during the transition process that flips dipoles and reverses the electric polarization. Ferroelectric FE(+) and FE(−) states are energetically degenerate eigenstates with opposite polarization direction.

stability of Tb_2CO_2 and Dy_2CO_2 based on their phonon spectra that are presented in Appendix A.

In the following text, we will focus on the electronic and the optical properties of M_2CO_2 structures in the α phase, which is more stable and exhibits nonzero electric polarization. As we discuss in Appendixes A and B, we find α-M_2CO_2 systems to be not only thermodynamically stable at room temperature but also dynamically stable even under moderate compressive strain.

B. Electronic structure and polarization behavior of $\alpha - Gd_2CO_2$

Metallic behavior of the layered 2D electride Gd_2C originates from itinerant electrons accumulated in between layers. Functionalizing the terminating layers with O engages unpaired electrons in new chemical bonds with the central C atoms. This changes the electronic structure of the system that is now free of itinerant electrons. As shown in Fig. 3(a), DFT calculations indicate that $\alpha - Gd_2CO_2$ turns to a semiconductor. We find the valence band maximum (VBM) at the K point and the conduction band minimum (CBM) at the Γ point, indicating an indirect band gap.

We should note here that the interpretation of Kohn-Sham eigenvalues as self-energies is strictly incorrect and that DFT-based band gaps are typically underestimated. We find this to be the case also when comparing band-gap values based on DFT-PBE and the hybrid DFT-HSE06 functional, which is believed to be superior to DFT-PBE in terms of optical spectra. The band gap of $\alpha - Gd_2CO_2$ is 1.17 eV based on DFT-PBE and 2.15 eV based on DFT-HSE06. As seen in Fig. 3(a), and as expected, the band dispersion is the same in both functionals. We find the same to be true also for the band structure of $\alpha - Tb_2CO_2$ and $\alpha - Dy_2CO_2$ discussed in Appendix C.

As mentioned above, the positively charged C atoms are displaced from their center position towards one of the terminating Gd layers in $\alpha - Gd_2CO_2$. As a result, the system acquires a macroscopic electric polarization in the out-of-plane direction. We use the standard Berry-phase method to calculate the polarization and obtain $P = 0.107$ pC/cm for $\alpha - Gd_2CO_2$. Similarly, we get $P = 0.113$ pC/cm for $\alpha - Tb_2CO_2$ and $P = 0.148$ pC/cm for $\alpha - Dy_2CO_2$.

C. Energy barrier for polarization reversal in ferroelectric $\alpha - Gd_2CO_2$

Since the origin of polarization in the α phase is a uniform displacement of the central C layer towards one of the terminating layers, the polarization can be reversed when the

C layer is displaced uniformly towards the other terminating layer, as can be simply inferred from Fig. 1(a). The possibility to reverse the polarization makes the α phase ferroelectric. Displacing alternatively every other C atom in one or the other direction leads to the β phase, shown in Fig. 1(b). The absence of net polarization in spite of nonzero alternating dipole moments makes the β phase antiferroelectric.

As mentioned, the polarization of the α phase could be reversed by displacing all C atoms at once, yielding an energetically degenerate α phase with opposite polarization. Rather than displacing all C atoms at once, the carbons could be shifted up or down alternatively, resulting in the β phase as a locally stable transition state. We illustrate this process from the α to the β phase in Fig. 3(b) using the unit cells that contain four C and four O atoms. Starting with the α phase, this transition starts by displacing only one O towards its closest C neighbor and attracting it to form a metastable state T. Similar displacement of the second O atom in the unit cell causes a transition to the β phase. The energy barrier ΔE associated with the polarization reversal process in $\alpha - Gd_2CO_2$ has been determined using the nudged elastic band (NEB) method and the results are shown in Fig. 3(c).

The barrier value 757 meV/unit cell for polarization reversal in Gd_2CO_2, which has been obtained in this way, is rather high. Even though this value is per unit cell and not per atom, it is significantly larger than $k_BT \approx 0.02$ eV/atom and thus should protect the polarization direction at room temperature. Applying an external field beyond the coercive field, a common way to reverse electric polarization in dielectrics, is unlikely to succeed in view of this high energy barrier. Not to dismiss this system as a dielectric based on the energy barrier alone, we wish to refer to a different system, a $LiNbO_3$-type corundum derivative $FeTiO_3$, with an even higher activation barrier of 763 meV/unit cell. In spite of this high barrier, ferroelectric behavior has been postulated in a theoretical study [45] and later on confirmed experimentally [46].

The approach we used to determine the activation barrier for polarization reversal is based on an artificial coherent process extending to the entire system, where every unit cell undergoes the change simultaneously. This view is oversimplified and clearly overestimates the barrier height to values unsurmountable at room temperature. As we expand upon in the Discussion section, the barrier in a realistic system, where the transition proceeds by defect motion that modifies domains, is significantly lower.

In Gd_2CO_2 and other related systems we consider here, we found that applied strain may change the energetically favored phase. As shown in Fig. 4, the energetically favored phase of Gd_2CO_2 changes from α to β under compressive strain $\varepsilon < \varepsilon_t$. Since the transition strain value $\varepsilon_t \approx -1.3\%$ in Gd_2CO_2 is relatively moderate, the possibility of phase stability reversal needs careful consideration when determining the effect of strain on the band structure, optical absorption and ferroelectric behavior of the system.

Even though the ferroelectric α phase becomes less stable than the β phase in the compression range associated with a direct band gap, it is protected from a spontaneous transition to the β phase by the above-mentioned high activation barrier. We have confirmed that even under compression, this activation barrier remains high, so the electronic and optical properties of ferroelectric $\alpha - Gd_2CO_2$ can be depended upon.

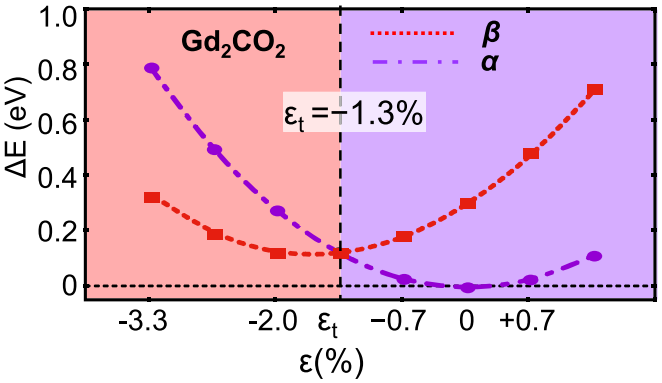

FIG. 4. Energy change ΔE as function of in-plane biaxial strain ε applied to the α and β phases of Gd_2CO_2, with $\varepsilon = 0$ referring to $\alpha - Gd_2CO_2$ in equilibrium. We emphasize the region where the α phase is more stable by the purple background and the region where the β phase is more stable by the red background. The dashed line at ε_t separates the regions where both phases are equally stable.

We have also performed analogous calculations for the other M_2CO_2 systems, Tb_2CO_2 and Dy_2CO_2. We report polarization changes in these systems in Appendix C and stability differences between the α and the β phase in Appendix D. We find these results to be very similar to those for Gd_2CO_2.

D. Effect of in-plane strain on the electronic properties and electric polarization of $\alpha - Gd_2CO_2$

It is well-known that lattice distortion can modify physical properties of materials. Applying external strain is a common way to modify the lattice structure. We use the common definition of strain $\varepsilon = \Delta a/a$. In this study, we apply in-plane biaxial strain on the 2D Gd_2CO_2 monolayer, with $-4\% < \varepsilon < +2\%$ to modify the the electronic band structure and the electric polarization. Before distorting the lattice, we investigated the energy needed to apply the strain and present our results in Fig. 5(a). Applying compressive strain of $\varepsilon = -4\%$ requires $\Delta E \approx 300$ meV/unit cell and applying tensile strain of $\varepsilon = +2\%$ costs $\Delta E \approx 60$ meV/unit cell. These values are close to those found in layered bulk black phosphorus [47], indicating similar mechanical properties.

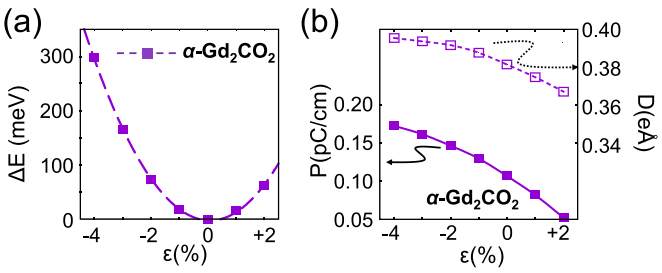

FIG. 5. (a) Energy changes ΔE as function of in-plane biaxial strain ε applied to $\alpha - Gd_2CO_2$. (b) Changes in the electric polarization P and the electric dipole D as function of in-plane biaxial strain ε applied to $\alpha - Gd_2CO_2$.

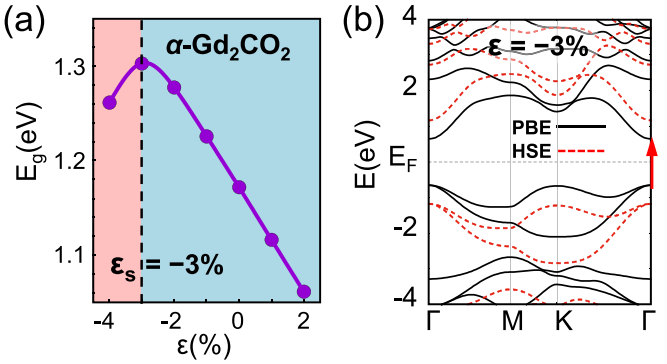

FIG. 6. (a) Dependence of the electronic band gap E_g on the in-plane biaxial strain ε. Compression beyond a specific value $\varepsilon_s < 0$ turns the system to a direct gap semiconductor. The direct gap semiconducting region $\varepsilon < \varepsilon_s$ is highlighted by pink and the indirect band gap region by light blue. (b) The electronic band structure $E(k)$ of $\alpha - Gd_2CO_2$ strained at $\varepsilon = \varepsilon_s$. Results based on the DFT-PBE functional are represented by the solid black line and results based on the DFT-HSE06 functional by the dashed red line.

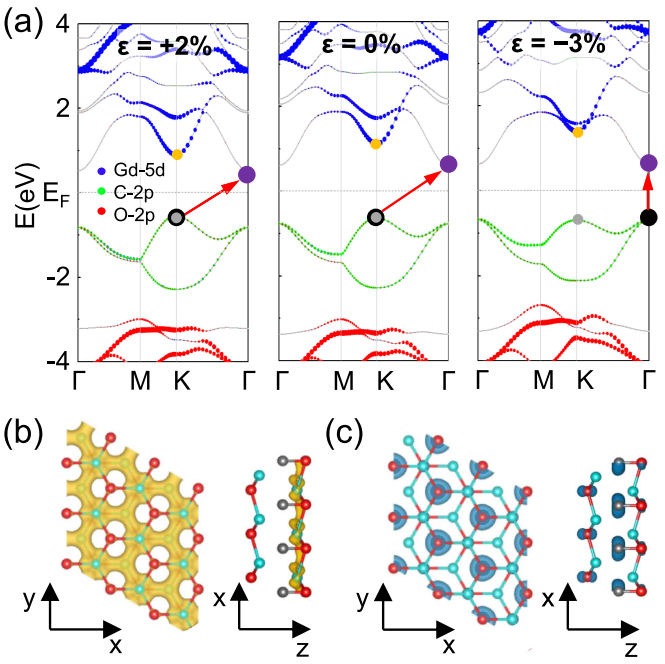

FIG. 7. (a) Orbital-projected electronic band structure $E(k)$ of $\alpha - Gd_2CO_2$ stretched by $\varepsilon = +2\%$, relaxed at $\varepsilon = 0\%$, and compressed by $\varepsilon = -3\%$. The CBM is indicated by the purple point and the VBM by the black point. At the K point, the conduction band eigenvalue is indicated by the yellow point and the valence band eigenvalue by the grey point. Isosurface charge density plots at the value $\rho = 0.035\, e/a_B^3$ represent the distribution of (b) conduction band electrons, shown in yellow, and (c) valence band electrons, shown in blue, at the K point in an unstrained structure.

Depending on applied strain, we find the off-center displacement Δd of C atoms in the middle layer to change along with the net Bader charge Q(C) of the C atoms. Electrons transferred from C to O atoms form an electrical dipole. We define this dipole by $D = Q(\mathrm{C}) \times \Delta d$ and present its dependence on the strain in Fig. 5(b). Independent of the estimated dipole value, we calculate the polarization P using the Berry phase method. We note different units but a similar dependence of P and D on the strain. There may be additional difference between the two quantities, since both the Bader charge analysis for D and the Berry phase method for P are approximations. As seen in Fig. 5(b), changing the strain from the tensile value $\varepsilon = +2\%$ to compression at $\varepsilon = -4\%$ causes a 333% increase of the polarization.

Also, the electronic band structure is susceptible to biaxial in-plane strain. As seen in Fig. 6(a), the band gap increases under compressive strain and decreases under tensile strain. At the specific compressive strain value $\varepsilon = \varepsilon_s = -3\%$, the band gap reaches its maximum and $\alpha - Gd_2CO_2$ turns from an indirect-gap to a direct-gap semiconductor. The band structure of $\alpha - Gd_2CO_2$ subject to ε_s strain is shown in Fig. 6(b). In comparison to the band structure of the unstrained system in Fig. 3(a), the CBM remains at the Γ point, but the VBM moves from the K point to the Γ point under in-plane compression. We observe the gap to decrease upon compression beyond ε_s, the switching point to a direct-gap semiconductor. The effect of biaxial strain on the band structure and polarization of $\alpha - Tb_2CO_2$ and $\alpha - Dy_2CO_2$ is discussed in Appendix E.

In the following, we analyze the mechanism underlying the transition from an indirect to a direct band gap due to in-plane strain in $\alpha - Gd_2CO_2$. We base our analysis on comparing the orbital-projected band structure of $\alpha - Gd_2CO_2$ at strain values $\varepsilon = +2\%$, $\varepsilon = 0\%$ and $\varepsilon = -3\%$ in Fig. 7(a). In comparison to the moderate changes at the VBM and CBM at the Γ point by strain, the corresponding changes at the K point are dramatic and worth further consideration.

As seen in Fig. 7(a), the character of the VBM and CBM at the K point consists mostly of C2p and Gd5d states. For the unstrained system, we display the K-point electron distribution at the CBM in Fig. 7(b) and at the VBM in Fig. 7(c). We find that CBM states at the K point consist mostly of hybridized Gd5d_{xy} and Gd5$d_{x^2-y^2}$ orbitals, which hybridize in covalent bonds between neighboring Gd atoms. The VBM at the K point, on the other hand, consists mainly of isolated C2p_x and C2p_y orbitals, which are responsible for forming covalent bonds between neighboring C atoms. As we show below, the Gd-Gd bonds in $\alpha - Gd_2CO_2$ are compressed and C–C bonds stretched with respect to their equilibrium values, which affects their behavior under strain.

The calculated Gd-Gd interatomic distance 3.77 Å in $\alpha - Gd_2CO_2$ turns out to be much smaller than the optimum value d_{opt}(Gd-Gd) = 4.56 Å found in bulk hcp-Gd [48], indicating that Gd-Gd bonds in the oxygenated carbide are under compression. Further compression should then move these states up in energy, away from the Fermi level. Still, the CBM remains at Γ.

On the other hand, the C–C interatomic distance d(C–C) = 3.77 Å in Gd_2CO_2 is much larger than the equilibrium length of C–C single bonds, d_{opt}(C–C) = 1.54 Å, and C=C double bonds, d_{opt}(C = C) = 1.45 Å [49]. Thus, carbon orbitals barely overlap in the oxygenated carbide and C–C bonds are under tension. Compression should lower the energy of the VBM, away from the Fermi level, even below its eigenvalue

at Γ. At some minimum compressive strain value ε_s, the maximum of the valence band moves from K to Γ and the band gap becomes direct.

E. Optical properties of $\alpha - Gd_2CO_2$

As discussed above, the $\alpha - Gd_2CO_2$ system can be turned into a direct-gap semiconductor by applying biaxial in-layer compressive strain. A direct band gap is highly desirable for optical applications, as it allows for a direct recombination of electrons in the conduction band with holes in the valence band, resulting in a high luminous efficiency. Even though the $E(k)$ dispersion relation is reproduced rather correctly by DFT-PBE, DFT is not designed to reproduce the fundamental band gap E_g and underestimates it significantly. Thus, for optical properties, we rely on the more appropriate DFT-HSE functional. Our study of the photon absorption properties of $\alpha - Gd_2CO_2$ is based on electronic-structure calculations using the DFT-HSE06 functional.

We determine the optical absorption coefficient $\alpha(\omega)$ from

$$\alpha(\omega) = \sqrt{2}\omega\sqrt{\left[\sqrt{\varepsilon_1^2 + \varepsilon_2^2} - \varepsilon_1\right]}/c, \tag{1}$$

where ω is the angular frequency and c is the speed of light. ε_1 is the real and ε_2 the imaginary part of the dielectric function, which can be calculated using

$$\varepsilon_2(\omega) = \frac{8\pi^2 e^2}{\omega^2 m^2} \sum_n \sum_{n'} \int |P^k_{nn'}|^2 f_{kn}(1 - f_{nn'}) \times \delta\left(E^k_n - E^k_{n'} - \frac{h\omega}{2\pi}\right) \frac{d^3k}{(2\pi)^3} \tag{2}$$

$$\varepsilon_1(\omega) = 1 + \frac{2P}{\pi} \int_0^\infty \frac{\omega' \varepsilon_2(\omega')}{\omega'^2 - \omega^2} d\omega' . \tag{3}$$

and Here, $P^k_{nn'}$ is the projection of elements of the momentum dipole matrix, f_{kn} is the Fermi-Dirac distribution, and $E^k_n(k)$ is the energy of the electron. m is the mass and e the charge of the electron.

Our results in Fig. 8(a) indicate that the absorption threshold of $\alpha - Gd_2CO_2$ under strain ε should occur near 2.5 eV, which is very close to the calculated band gap. We should expect no optical absorption below the corresponding frequency. We can identify five strong absorption peaks in the range from $5 - 20$ eV. Two of these can be associated with the ultraviolet spectrum of carbon in the energy range from $4.4 - 12.4$ eV. The strongest three peaks occur in the extreme-ultraviolet range of the optical spectrum ranging from $10.25 - 124$ eV.

As seen in Fig. 8(a), the calculated absorption spectra $\alpha(\omega)$ are the same in the x and y directions, indicating that the absorption should be isotropic. This is caused by the energetic degeneracy of C2p_x and C2p_y, Gd5d_{xy} and Gd5$d_{x^2-y^2}$, Gd5d_{xz} and Gd5d_{yz} states that can be understood using group theory. As mentioned above, the space group of $\alpha - M_2CO_2$ structures is $P3m1$ and the point group is C_{3v}. The linear function of (x, y), quadratic function of $(x^2 - y^2, xy)$ and (xz, yz) belong to the E irreducible representation of the C_{3v} group, which means that p_x and p_y are degenerate in energy, same as d_{xy}, $d_{x^2-y^2}$, d_{xz}, and d_{yz} are degenerate in energy.

To confirm our interpretation, we analyzed the total density of states by plotting the partial density of states (PDOS)

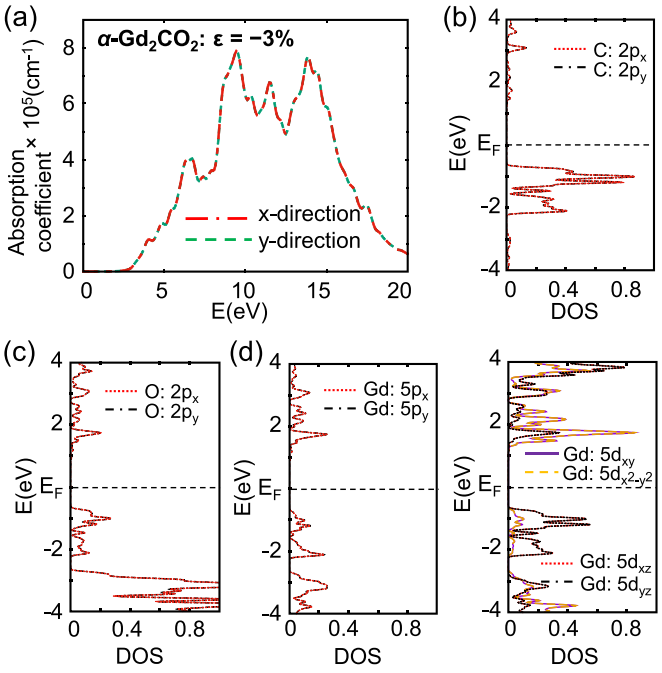

FIG. 8. (a) The optical absorption coefficient of $\alpha - Gd_2CO_2$ subject to isotropic strain $\varepsilon = -3\%$. Electronic density of states projected on (b) $2p_x$ and $2p_y$ states of C atoms, (c) $2p_x$ and $2p_y$ states of O atoms, and (d) $5p_x$, $5p_y$, $5d_{xy}$, $5d_{x^2-y^2}$, $5d_{xz}$, and $5d_{yz}$ states of Gd atoms.

associated with the elements present in the structure and display our results in Figs. 8(b)–8(d). Our PDOS results show that the p_x and p_y states of C, O, and Gd atoms are identical. Similarly, we find the Gd5d_{xy} and Gd5$d_{x^2-y^2}$, the Gd5d_{xz} and Gd5d_{yz} eigenstates to be identical. Thus, the electronic behavior of Gd_2CO_2 is the same in the x and y directions, meaning it is isotropic.

As further discussed in Appendix F, we also find the absorption spectra of Tb_2CO_2 and Dy_2CO_2 under compression to be the same in the x and y directions and thus isotropic. To make sure that these structures do not collapse under the compressive strain, we first calculated their phonon spectra. As we further expand on in Appendix A, we confirmed the stability of these structures under compression by absence of imaginary frequencies in their phonon spectra.

IV. DISCUSSION

As we know, Gd is a rare-earth element in the lanthanide series. Since rare-earth elements are heavy, we expect spin-orbit coupling (SOC) to play a significant role in the band structure and possibly to also affect significantly the optical properties. We have investigated this point in Appendix G and find that SOC does split bands, yet the split is very small at the VBM and CBM, which dominate the optical response. We conclude that SOC effects play only a minor role in optical properties of the M_2CO_2 systems of interest here.

Bulk Gd is ferromagnetic (FM) below the Curie temperature $T_C = 20°C$. Also, the 2D electride Gd_2C turns out to be ferromagnetic [17]. Even though we have not touched upon magnetism in this study of the electronic properties, we still

may ask, whether there may be magnetic order in Gd_2CO_2. A related question may be, whether any magnetic order in the system may affect ferroelectricity. Not providing sufficient depth in a corresponding study, we considered the possibility of FM and anitferromagnetic (AFM) ordering in the system.

Assuming FM order, we found that Gd in Gd_2CO_2 carries a magnetic moment of $7\,\mu_B$, which is close to its measured local moment of $7.26\,\mu_B$ in Gd_2C [50]. Assuming AFM order, the magnetic moments of Gd atoms in the terminating layers point in opposite directions. Assuming any of these magnetic orders, we find the α phase to still be most stable and the atomic structure to be nearly identical to the nonmagnetic structure. The magnetic properties of Gd_2CO_2 originate in the Gd4f electrons. In comparison to the Gd5d and Gd6s electrons, Gd4f electrons reside in the inner shell of the atom and thus do not contribute to chemical bonding. Thus, the effect of magnetic order on the atomic structure and also the ferroelectric behavior can be ignored. Also, the Gd4f electrons are deep below the Fermi level. Hence, the optical properties are not affected by the magnetic order to a significant level.

The microscopic transition from the α to the β phase, depicted in Figs. 1 and 3(b), involves C atoms in the middle layer. In the Gd_2C system, these atoms are equidistant to Gd atoms in the terminating layers. This situation, however, changes with oxidation. As O atoms attach to the Gd atoms, the single-well potential of the C atoms changes to a double-well potential and the system gains energy when the C atoms move closer to one or the other terminating layer. This symmetry breaking results in the formation of electric dipoles that are responsible for ferroelectricity and change the system to an indirect gap semiconductor.

We expect that the transition from a single-well to a double-well potential is not limited to oxygen termination but may well occur with other functional groups such as hydroxyls. Unlike oxygen atoms, hydroxyl groups carry an electric dipole that may, upon proper alignment, give rise to in-plane ferroelectricity. While this consideration exceeds the scope of our paper, we anticipate that combining M_2C with other functional groups may lead to other types of behavior of interest for applications.

Next we wish to revisit the high value of the activation barrier for polarization reversal in the M_2CO_2 systems. As in all phase changes, polarization reversal is a complex process that usually involves nucleation and motion of defects and requires significantly lower activation barriers than those estimated for the artificial coherent process considered here. Whereas the nature of specific defects is a complex problem beyond the scope of our paper, this topic has been discussed before in a different, simpler system and context. In elemental selenium, so-called point-dislocation motion has been shown to significantly lower the activation barrier for the transformation of a one-dimensional Se helix to a two-dimensional allotrope [51].

Similar to the example of defective Se, the M_2CO_2 systems have been formed at nonzero temperature. They will also be nonuniform, but rather contain coexisting α and β phase domains, separated by domain walls. At whatever applied strain value, the fraction of the dominant phase will depend on the free-energy difference. The transition barrier value we calculated would matter only in the artificial pure phase. In the common case of phase coexistence, we expect significant lowering of the energy barriers for moving dislocations along domain-wall boundaries and will change the fraction of the dominant phase according to free-energy differences.

Unlike in many other electrides, we report in Fig. 4 that external strain may change the energetically favored phase from the ferroelectric $\alpha - M_2CO_2$ to the antiferroelectric β phase. In our opinion, this interesting aspect of the the system may be used in our favor. Even though each phase is protected by a substantial activation barrier, we expect this barrier to generally decrease in a strained system. We can imagine that subjecting the α phase temporarily to a specific compressive strain may accelerate a transition to the β phase and, eventually, to a ferroelectric α phase with reversed polarization under applied electric field. Lowering the ambient temperature and adjusting the applied strain should then stabilize $\alpha - M_2CO_2$ with the reversed polarization.

Since our study is a theoretical prediction for M_2CO_2 structures that have not been synthesized yet, we may only speculate and provide hopefully valuable hints to experimentalists interested in procuring them. Except for the successful synthesis of bulk M_2C [33,52], there is only scarce information available on how these structures may behave in different environments. We feel that M_2C monolayers may behave similar to structurally and chemically related MXenes, which have been investigated extensively. Traditional etching with HF has been shown to lead to $-$F termination [53], and alkalization to lead to $-$OH termination [54]. Heating under an inert atmosphere has converted $-$OH termination to $-$O termination [55]. Thus, we feel that techniques used to oxidize MXenes may also be used to form M_2CO_2 structures.

V. SUMMARY AND CONCLUSIONS

In this paper, we investigated the physical properties of oxygen-terminated carbides of lanthanide elements with the composition M_2CO_2, which form 2D structures. Our calculations reveal two dynamically stable phases of these compounds, namely, the energetically favored ferroelectric α phase with an out-of-plane polarization, and the antiferroelectric β phase. Applying in-plane biaxial strain changes the ferroelectric polarization of the α phase in a linear fashion and modifies the size and nature of the fundamental band gap from direct to indirect. We also find that the relative stability of the α and the β phases can be changed by applying in-plane biaxial strain. In structures with a direct band gap, found in the compressive regime, the in-plane electronic properties are the same in the x and y directions. Thus, the optical properties turn isotropic and exhibit excellent photon absorption in the ultraviolet range. We believe that this previously unexplored class of systems should find unique applications among optoelectronic materials.

ACKNOWLEDGMENTS

L.H., P.L., and D.L. acknowledge financial support from the Natural Science Foundation of the Jiangsu Province Grant No. BK20210198, the National Natural Science Foundation of China (NNSFC) Grant No. 12204095, the High Level Personnel Project of Jiangsu Provience Grant No. JSSCBS20220120, and the Zhishan Foundation of Southeast University

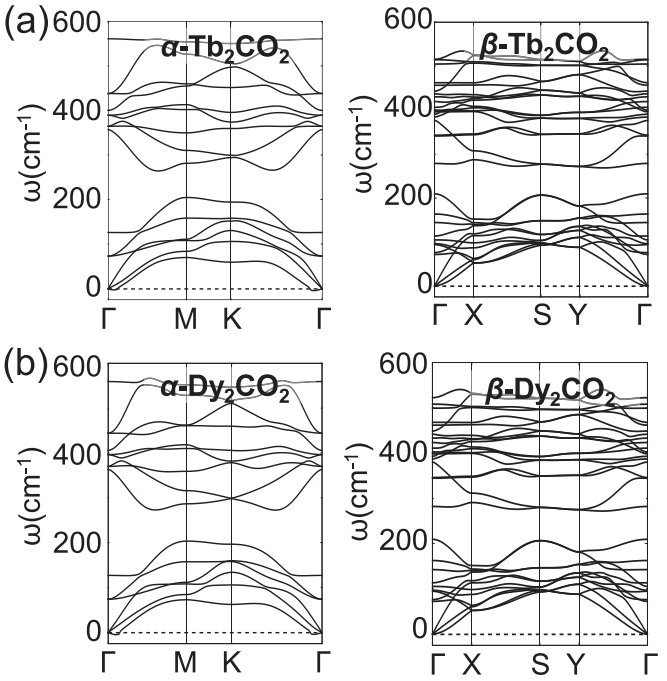

FIG. 9. Phonon spectra of the equilibrated α and β phases of (a) Tb_2CO_2 and (b) Dy_2CO_2.

Grant No. 2242023R10006. X.L. acknowledges financial support by NNSFC Grant No. 11974312.

APPENDIX A: DYNAMIC STABILITY OF RELAXED AND COMPRESSED Gd_2CO_2, Tb_2CO_2, AND Dy_2CO_2

Calculated phonon spectra of unstrained Tb_2CO_2 and Dy_2CO_2 in the α and β phases, with the structures depicted in Fig. 1, are presented in Fig. 9.

Calculated phonon spectra of Gd_2CO_2, Tb_2CO_2, and Dy_2CO_2 subject to compressive strain in the value range of interest for for optical properties, namely, $\varepsilon = -3\%$ in Gd_2CO_2, $\varepsilon = -2\%$ in Tb_2CO_2, and $\varepsilon = -1.5\%$ in Dy_2CO_2, are presented in Fig. 10.

All spectra are free of imaginary frequencies, meaning that irrespective of compression, the 2D M_2CO_2 (M = Gd, Dy and Tb) structures are dynamically stable.

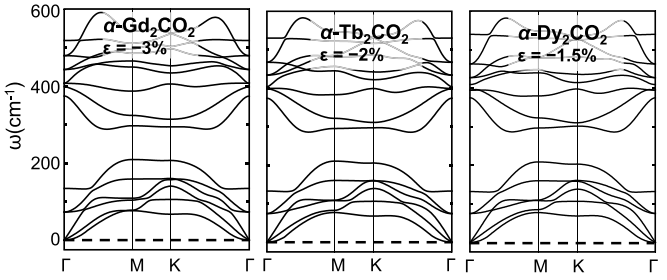

FIG. 10. Phonon spectra of 2D M_2CO_2 systems under compressive strain $\varepsilon < 0$. Results are presented for (a) $\alpha - Gd_2CO_2$ at $\varepsilon = -3\%$, (b) $\alpha - Tb_2CO_2$ at $\varepsilon = -2\%$, and (c) $\alpha - Dy_2CO_2$ at $\varepsilon = -1.5\%$.

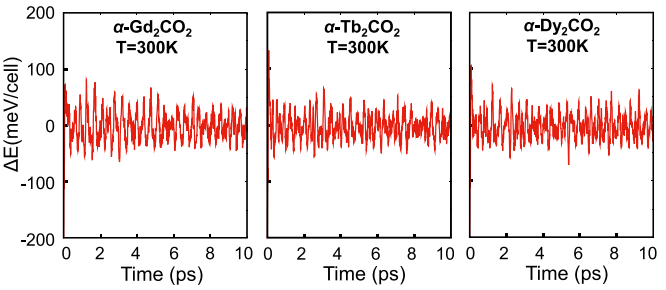

FIG. 11. Changes in the potential energy ΔE per unit cell of (a) $\alpha - Gd_2CO_2$, (b) $\alpha - Tb_2CO_2$, and (c) $\alpha - Dy_2CO_2$ during a 10-ps long canonical MD simulation run at $T = 300$ K.

APPENDIX B: THERMODYNAMIC STABILITY OF M_2CO_2 IN THE α PHASE

To study the thermodynamic stability of M_2CO_2 structures, we have performed canonical molecular dynamics simulations of the α phase at room temperature ($T = 300$ K) for a time period of 10 ps. As seen in Fig. 11, the potential energy fluctuates around a constant value, indicating that all structures are dynamically stable at room temperature.

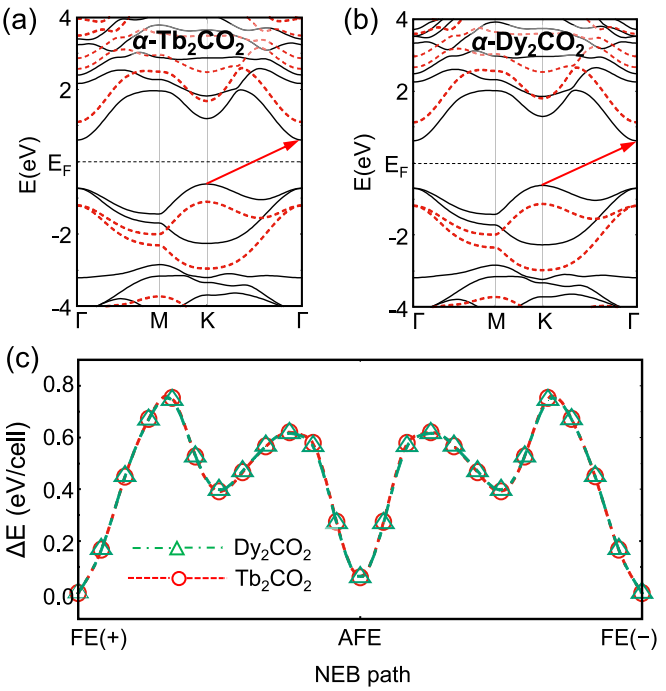

FIG. 12. Electronic band structure $E(k)$ of (a) $\alpha - Tb_2CO_2$ and (b) $\alpha - Dy_2CO_2$. DFT-PBE results are represented by the solid black lines and DFT-HSE06 results by the dashed red lines. (c) Energy changes ΔE per unit cell during the transition process that flips dipoles and reverses the polarization of $\alpha - Tb_2CO_2$ and $\alpha - Dy_2CO_2$. The process is very similar to $\alpha - Gd_2CO_2$, as seen in Fig. 3.

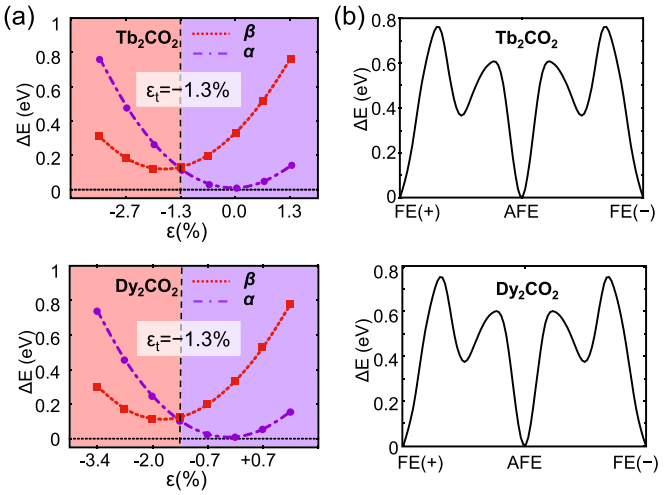

FIG. 13. (a) Energy changes ΔE in the α and β phases of Tb_2CO_2 and Dy_2CO_2 as a function of applied in-plane biaxial strain ε. The region where the α phase is more stable is indicated by the purple background and the region, where the β phase is more stable by the red background. Equal stability of both phases at ε_t is indicated by the dashed line, which separates the two regions. (b) Energy changes ΔE along the transformation path from the $\alpha-$ to the β phase of $\alpha - Tb_2CO_2$ and $\alpha - Dy_2CO_2$ at the strain value ε_t.

APPENDIX C: BAND STRUCTURE AND POLARIZATION CHANGES IN Tb_2CO_2 AND Dy_2CO_2

Results of our band structure calculations with the DFT-PBE and DFT-HSE06 functionals are shown in Fig. 12(a) for $\alpha - Tb_2CO_2$ and in Fig. 12(b) for $\alpha - Dy_2CO_2$. Our results indicate that both systems are indirect-gap semiconductors. The DFT-PBE-based band gap is surely underestimated at 1.22 eV for $\alpha - Tb_2CO_2$ and 1.24 eV for $\alpha - Dy_2CO_2$. Values based on DFT-HSE06, 2.22 eV for $\alpha - Tb_2CO_2$ and 2.27 eV for $\alpha - Dy_2CO_2$, are likely better estimates for the optical band gap.

The energetics of the process that flips dipoles and reverses the polarization, presented in Fig. 3(b) for $\alpha - Gd_2CO_2$, is shown in Fig. 12(c) for $\alpha - Tb_2CO_2$ and $\alpha - Dy_2CO_2$.

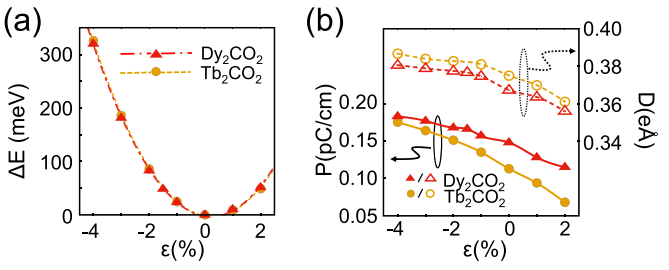

FIG. 14. (a) Energy changes ΔE per unit cell as function of in-plane biaxial strain ε applied to $\alpha - Tb_2CO_2$ and $\alpha - Dy_2CO_2$. (b) Electric polarization P and dipole moment D of Tb_2CO_2 and Dy_2CO_2 as a function of the in-plane biaxial strain ε. Results for the two systems are distinguished by the color and the symbols.

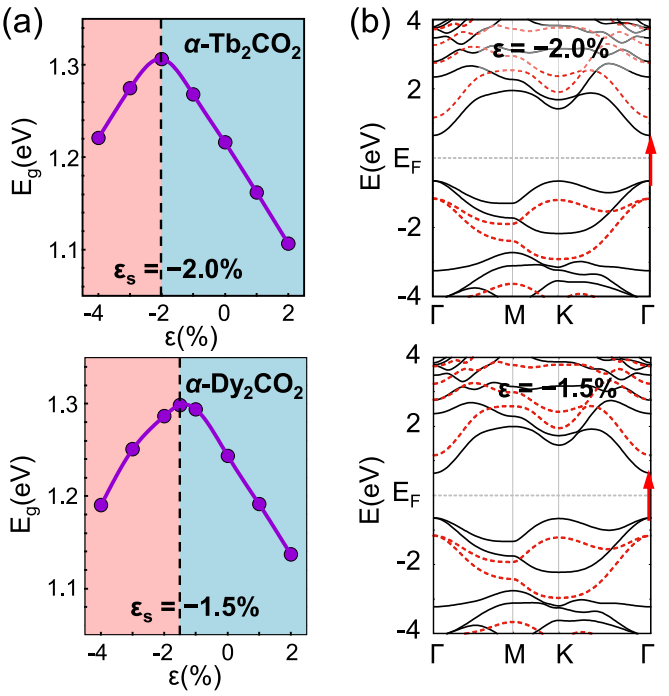

FIG. 15. (a) Dependence of the electronic band gap E_g on the in-plane biaxial strain ε in $\alpha - Tb_2CO_2$ and $\alpha - Dy_2CO_2$. Both systems change from indirect-gap to direct-gap semiconductors at compressive strains $\varepsilon < \varepsilon_s$. The direct-gap region at high compression is indicated by the pink background and the indirect-gap region by light blue. (b) The electronic bands structure $E(k)$ of $\alpha - Tb_2CO_2$ and $\alpha - Dy_2CO_2$ subject to specific strain values ε. Results based on the DFT-PBE functional are represented by solid black lines and those based on DFT-HSE06 are shown by dashed red lines.

APPENDIX D: RELATIVE STABILITY OF THE α AND β PHASES OF Tb_2CO_2 AND Dy_2CO_2

As mentioned in the main text, at strain values below $\varepsilon_t \approx -1.3\%$ in the compressive regime, the β phase of Gd_2CO_2 becomes more stable than the α phase. We see in Fig. 13(a) that the transition strain maintains its value $\varepsilon_t \approx -1.3\%$ also in Tb_2CO_2 and Dy_2CO_2. Energy changes along the transformation path from the α to the β phase, shown in Fig. 13(b), indicate a similar energy barrier around 750 meV in Tb_2CO_2 and Dy_2CO_2 to that found in Gd_2CO_2.

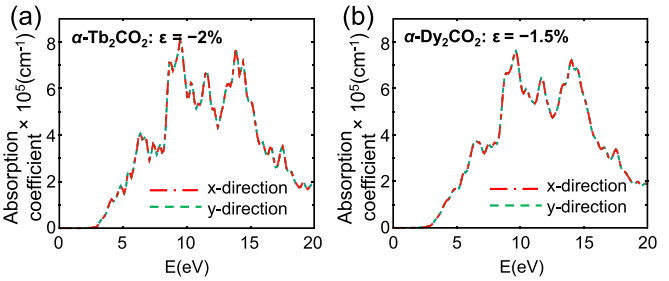

FIG. 16. Optical absorption spectra of (a) $\alpha - Tb_2CO_2$ at $\varepsilon = -2\%$ and (b) $\alpha - Dy_2CO_2$ at $\varepsilon = -1.5\%$, where both systems become direct-gap semiconductors.

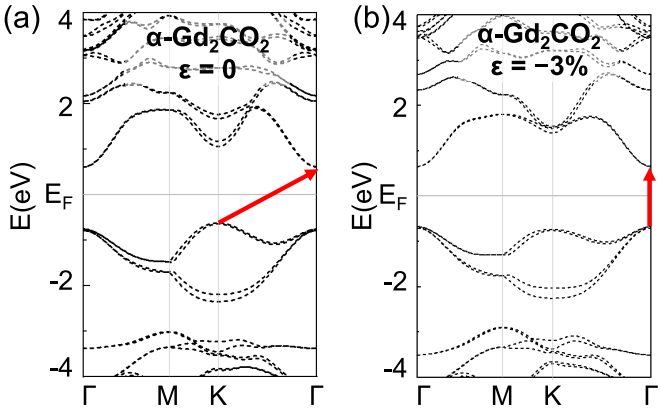

FIG. 17. Electronic band structure $E(k)$ of α-Gd_2CO_2 subject to (a) no strain and (b) compressive strain $\varepsilon = -3\%$. The calculations, which consider spin-orbit coupling, are based on the DFT-PBE functional.

APPENDIX E: STRAIN EFFECT ON THE ELECTRONIC STRUCTURE AND POLARIZATION OF Tb_2CO_2 AND Dy_2CO_2

Energy changes caused by applying in-plane biaxial strain to $\alpha - Tb_2CO_2$ and $\alpha - Dy_2CO_2$ are shown in Fig. 14(a). As seen in Fig. 14(b) and similar to $\alpha - Gd_2CO_2$, the electric polarization and dipole moment of Tb_2CO_2 and Dy_2CO_2 increase with increasing compressive strain and decrease with increasing tensile strain. Changing from tensile strain $\varepsilon = +2\%$ to compressive strain $\varepsilon = -4\%$ increases the polarization by 257% in $\alpha - Tb_2CO_2$ and by 159% in $\alpha - Dy_2CO_2$.

Changes in the band gap of $\alpha - Tb_2CO_2$ and $\alpha - Dy_2CO_2$ as a function of biaxial in-plane strain are shown in Fig. 15(a). At the compressive strain values $\varepsilon_s = -2.0\%$ for $\alpha - Tb_2CO_2$ and $\varepsilon_s = -1.5\%$ for $\alpha - Dy_2CO_2$, both systems turn into direct-gap semiconductors. Their band structure at the strain value ε_s is shown in Fig. 15(b).

APPENDIX F: OPTICAL ABSORPTION OF Tb_2CO_2 AND Dy_2CO_2

Calculated optical absorption spectra of Tb_2CO_2 and Dy_2CO_2 at the specific biaxial in-plane strain value ε, where they become direct-gap semiconductors, are shown in Fig. 16. Similar to Gd_2CO_2, the absorption spectra of Tb_2CO_2 and Dy_2CO_2 are characterized by five absorption peaks in the range between 5 eV and 20 eV. Two of these peaks are associated with the UV spectrum of carbon, and the other three belong to the extreme-ultraviolet spectrum.

APPENDIX G: EFFECT OF SPIN-ORBIT COUPLING ON THE ELECTRONIC BAND STRUCTURE OF RELAXED AND STRAINED Gd_2CO_2

We have calculated the effect of spin-orbit coupling (SOC) on the electronic structure of unstrained and compressed Gd_2CO_2 using the DFT-PBE functional. As seen in Fig. 17, SOC does cause band splitting. However, the splitting is very small at the VBM and CBM, which remain at the Γ point under compressive strain. Since the electronic structure at the VBM and CBM dominates the optical properties, we conclude that the corresponding calculation does not require specific consideration of SOC effects in M_2CO_2 monolayers.

[1] Meeting Report, Minutes of the Washington Meeting, April 23 and 24, 1920, Phys. Rev. **15**, 505 (1920).

[2] J. Valasek, Piezo-electric and allied phenomena in Rochelle salt, Phys. Rev. **17**, 475 (1921).

[3] W. Ding, J. Zhu, Z. Wang, Y. Gao, D. Xiao, Y. Gu, Z. Zhang, and W. Zhu, Prediction of intrinsic two-dimensional ferroelectrics in In_2Se_3 and other III_2-VI_3 van der Waals materials, Nat. Commun. **8**, 14956 (2017).

[4] Y. Zhou, D. Wu, Y. Zhu, Y. Cho, Q. He, X. Yang, K. Herrera, Z. Chu, Y. Han, M. C. Downer, H. Peng, and K. Lai, Out-of-plane piezoelectricity and ferroelectricity in layered α-In_2Se_3 nanoflakes, Nano Lett. **17**, 5508 (2017).

[5] A. Belianinov, Q. He, A. Dziaugys, P. Maksymovych, E. Eliseev, A. Borisevich, A. Morozovska, J. Banys, Y. Vysochanskii, and S. V. Kalinin, $CuInP_2S_6$ room temperature layered ferroelectric, Nano Lett. **15**, 3808 (2015).

[6] F. Liu, L. You, K. L. Seyler, X. Li, P. Yu, J. Lin, X. Wang, J. Zhou, H. Wang, H. He, S. T. Pantelides, W. Zhou, P. Sharma, X. Xu, P. M. Ajayan, J. Wang, and Z. Liu, Room-temperature ferroelectricity in $CuInP_2S_6$ ultrathin flakes, Nat. Commun. **7**, 12357 (2016).

[7] D. Liu, L. Han, R. Wei, S. Song, J. Guan, S. Dong, and D. Tománek, Unusual electric polarization behavior in elemental quasi-two-dimensional allotropes of selenium, Phys. Rev. Mater. **6**, 103403 (2022).

[8] M. Wu, J. D. Burton, E. Y. Tsymbal, X. C. Zeng, and P. Jena, Hydroxyl-decorated graphene systems as candidates for organic metal-free ferroelectrics, multiferroics, and high-performance proton battery cathode materials, Phys. Rev. B **87**, 081406(R) (2013).

[9] K. Lee, S. W. Kim, Y. Toda, S. Matsuishi, and H. Hosono, Dicalcium nitride as a two-dimensional electride with an anionic electron layer, Nature (London) **494**, 336 (2013).

[10] Y. Lu, J. Li, T. Tada, Y. Toda, S. Ueda, T. Yokoyama, M. Kitano, and H. Hosono, Water durable electride Y_5Si_3: Electronic structure and catalytic activity for ammonia synthesis, J. Am. Chem. Soc. **138**, 3970 (2016).

[11] J. Wang, K. Hanzawa, H. Hiramatsu, J. Kim, N. Umezawa, K. Iwanaka, T. Tada, and H. Hosono, Exploration of stable strontium phosphide-based electrides: Theoretical structure prediction and experimental validation, J. Am. Chem. Soc. **139**, 15668 (2017).

[12] Y. Lu, J. Wang, J. Li, J. Wu, S. Kanno, T. Tada, and H. Hosono, Realization of Mott-insulating electrides in dimorphic Yb_5Sb_3, Phys. Rev. B **98**, 125128 (2018).

[13] C. Liu, S. A. Nikolaev, W. Ren, and L. A. Burton, Electrides: A review, J. Mater. Chem. C **8**, 10551 (2020).

[14] D. L. Druffel, K. L. Kuntz, A. H. Woomer, F. M. Alcorn, J. Hu, C. L. Donley, and S. C. Warren, Experimental demonstration of an electride as a 2D material, J. Am. Chem. Soc. **138**, 16089 (2016).

[15] X. Zhang, Z. Xiao, H. Lei, Y. Toda, S. Matsuishi, T. Kamiya, S. Ueda, and H. Hosono, Two-dimensional transition-metal electride Y_2C, Chem. Mater. **26**, 6638 (2014).

[16] Y. Oh, J. Lee, J. Park, H. Kwon, I. Jeon, S. W. Kim, G. Kim, S. Park, and S. W. Hwang, Electric field effect on the electronic structure of 2D Y_2C electride, 2D Mater. **5**, 035005 (2018).

[17] S. Y. Lee, J.-Y. Hwang, J. Park, C. N. Nandadasa, Y. Kim, J. Bang, K. Lee, K. H. Lee, Y. Zhang, Y. Ma, H. Hosono, Y. H. Lee, S.-G. Kim, and S. W. Kim, Ferromagnetic quasi-atomic electrons in two-dimensional electride, Nat. Commun. **11**, 1526 (2020).

[18] L. M. McRae, R. C. Radomsky, J. T. Pawlik, D. L. Druffel, J. D. Sundberg, M. G. Lanetti, C. L. Donley, K. L. White, and S. C. Warren, Sc_2C, a 2D semiconducting electride, J. Am. Chem. Soc. **144**, 10862 (2022).

[19] H. Huang, K.-H. Jin, S. Zhang, and F. Liu, Topological electride Y_2C, Nano Lett. **18**, 1972 (2018).

[20] J. Park, J.-Y. Hwang, K. H. Lee, S.-G. Kim, K. Lee, and S. W. Kim, Tuning the spin-alignment of interstitial electrons in two-dimensional Y_2C electride via chemical pressure, J. Am. Chem. Soc. **139**, 17277 (2017).

[21] K. Horiba, R. Yukawa, T. Mitsuhashi, M. Kitamura, T. Inoshita, N. Hamada, S. Otani, N. Ohashi, S. Maki, J. I. Yamaura, H. Hosono, Y. Murakami, and H. Kumigashira, Semimetallic bands derived from interlayer electrons in the quasi-two-dimensional electride Y_2C, Phys. Rev. B **96**, 045101 (2017).

[22] X.-L. Qiu, J.-F. Zhang, H.-C. Yang, Z.-Y. Lu, and K. Liu, Superconductivity in monolayer Ba_2N electride: First-principles study, Phys. Rev. B **105**, 165101 (2022).

[23] G. Wang, Z. Ma, J.-W. Jiang, J.-K. Yang, Y.-L. Sun, Z.-F. Qian, P. Huang, P. Zhang, and S.-H. Wei, Crystal structures and physicochemical properties of Be_2N and Mg_2N as electride materials, Phys. Rev. Appl. **19**, 034014 (2023).

[24] D. Wang, H. Li, L. Zhang, Z. Sun, D. Han, L. Niu, X. Zhong, X. Qu, and L. Yang, First-principles study on OH-functionalized 2D electrides: $Ca_2N(OH)$ and $Y_2C(OH)_2$, promising two-dimensional monolayers for metal-ion batteries, Appl. Surf. Sci. **478**, 459 (2019).

[25] L. Zhou, Y. Zhang, Z. Zhuo, A. J. Neukirch, and S. Tretiak, Interlayer-decoupled SC-based MXene with high carrier mobility and strong light-harvesting ability, J. Phys. Chem. Lett. **9**, 6915 (2018).

[26] L. Hong, R. F. Klie, and S. Öğüt, First-principles study of size- and edge-dependent properties of MXene nanoribbons, Phys. Rev. B **93**, 115412 (2016).

[27] L. Li, Effects of the interlayer interaction and electric field on the band gap of polar bilayers: A case study of Sc_2CO_2, J. Phys. Chem. C **120**, 24857 (2016).

[28] J. Hu, B. Xu, C. Ouyang, S. A. Yang, and Y. Yao, Investigations on V_2C and V_2CX_2 (X = F, OH) monolayer as a promising anode material for Li ion batteries from first-principles calculations, J. Phys. Chem. C **118**, 24274 (2014).

[29] M. Khazaei, A. Ranjbar, M. Ghorbani-Asl, M. Arai, T. Sasaki, Y. Liang, and S. Yunoki, Nearly free electron states in MXenes, Phys. Rev. B **93**, 205125 (2016).

[30] K. Maeda, H. Wakayama, Y. Washio, A. Ishikawa, M. Okazaki, H. Nakata, and S. Matsuishi, Visible-light-induced photocatalytic activity of stacked MXene sheets of Y_2CF_2, J. Phys. Chem. C **124**, 14640 (2020).

[31] Z. K. Baghini, A. Mostafaei, and M. Abbasnejad, Y_2CF_2 and Lu_2CF_2 MXenes under applied strain: Electronic, optical, and photocatalytic properties, J. Alloys Compd. **922**, 166198 (2022).

[32] Z. Wang, N. Ding, C. Gui, S.-S. Wang, M. An, and S. Dong, Ferroelectricity in strained Hf_2CF_2 monolayer, Phys. Rev. Mater. **5**, 074408 (2021).

[33] D. Xu, J.-F. Zhang, Z.-Y. Lu, and K. Liu, Magnetic and electronic transitions in monolayer electride induced by hydrogenation: A first-principles study, Phys. Rev. B **106**, 045138 (2022).

[34] J. Bu, H. Wu, J. Xu, and S. Zhang, Tuning the magnetic properties of two-dimensional electride Gd_2C via halogenation, J. Phys. Chem. C **127**, 14962 (2023).

[35] G. Kresse and J. Furthmüller, Efficient iterative schemes for *ab initio* total-energy calculations using a plane-wave basis set, Phys. Rev. B **54**, 11169 (1996).

[36] G. Kresse and D. Joubert, From ultrasoft pseudopotentials to the projector augmented-wave method, Phys. Rev. B **59**, 1758 (1999).

[37] J. P. Perdew, K. Burke, and M. Ernzerhof, Generalized gradient approximation made simple, Phys. Rev. Lett. **77**, 3865 (1996).

[38] J. Heyd, G. E. Scuseria, and M. Ernzerhof, Hybrid functionals based on a screened Coulomb potential, J. Chem. Phys. **118**, 8207 (2003).

[39] J. Heyd, G. E. Scuseria, and M. Ernzerhof, Erratum: "Hybrid functionals based on a screened Coulomb potential" [J. Chem. Phys. 118, 8207 (2003)], J. Chem. Phys. **124**, 219906 (2006).

[40] H. J. Monkhorst and J. D. Pack, Special points for Brillouin-zone integrations, Phys. Rev. B **13**, 5188 (1976).

[41] M. R. Hestenes and E. Stiefel, Methods of conjugate gradients for solving linear systems, J. Res. Natl. Bur. Stan. **49**, 409 (1952).

[42] R. D. King-Smith and D. Vanderbilt, Theory of polarization of crystalline solids, Phys. Rev. B **47**, 1651 (1993).

[43] R. Resta, Macroscopic polarization in crystalline dielectrics: The geometric phase approach, Rev. Mod. Phys. **66**, 899 (1994).

[44] A. Togo and I. Tanaka, First principles phonon calculations in materials science, Scr. Mater. **108**, 1 (2015).

[45] M. Ye and D. Vanderbilt, Ferroelectricity in corundum derivatives, Phys. Rev. B **93**, 134303 (2016).

[46] T. Varga, A. Kumar, E. Vlahos, S. Denev, M. Park, S. Hong, T. Sanehira, Y. Wang, C. J. Fennie, S. K. Streiffer, X. Ke, P. Schiffer, V. Gopalan, and J. F. Mitchell, Coexistence of weak ferromagnetism and ferroelectricity in the high pressure $LiNbO_3$-type phase of $FeTiO_3$, Phys. Rev. Lett. **103**, 047601 (2009).

[47] J. Guan, W. Song, L. Yang, and D. Tománek, Strain-controlled fundamental gap and structure of bulk black phosphorus, Phys. Rev. B **94**, 045414 (2016).

[48] H. Zeng, J. Zhang, C. Kuang, and M. Yue, Magnetic entropy change in bulk nanocrystalline Gd metals, Appl. Nanosci. **1**, 51 (2011).

[49] L. Pauling, L. O. Brockway, and J. Y. Beach, The dependence of interatomic distance on single bond-double bond resonance, J. Am. Chem. Soc. **57**, 2705 (1935).

[50] Y. Mudryk, D. Paudyal, V. K. Pecharsky, and K. A. Gschneidner, Magnetic properties of Gd_2C: Experiment and first principles calculations, J. Appl. Phys. **109**, 07A924 (2011).

[51] D. Liu, X. Lin, and D. Tománek, Microscopic mechanism of the helix-to-layer transformation in elemental group VI solids, Nano Lett. **18**, 4908 (2018).

[52] X. Zhang, S. Matsuishi, and H. Hosono, Critical behavior and magnetocaloric effect in layered structure Tb_2C, J. Phys. D: Appl. Phys. **49**, 335002 (2016).

[53] S. Li, P. Tuo, J. Xie, X. Zhang, J. Xu, J. Bao, B. Pan, and Y. Xie, Ultrathin MXene nanosheets with rich fluorine termination groups realizing efficient electrocatalytic hydrogen evolution, Nano Energy **47**, 512 (2018).

[54] Y. Xie, M. Naguib, V. N. Mochalin, M. W. Barsoum, Y. Gogotsi, X. Yu, K.-W. Nam, X.-Q. Yang, A. I. Kolesnikov, and P. R. C. Kent, Role of surface structure on Li-ion energy storage capacity of two-dimensional transition-metal carbides, J. Am. Chem. Soc. **136**, 6385 (2014).

[55] M. Lu, H. Li, W. Han, J. Chen, W. Shi, J. Wang, X.-M. Meng, J. Qi, H. Li, B. Zhang, W. Zhang, and W. Zheng, 2D titanium carbide (MXene) electrodes with lower-F surface for high performance lithium-ion batteries, J. Energy Chem. **31**, 148 (2019).